2015

Uncertainty quantification of an effective heat transfer coefficient within a numerical model of a bubbling fluidized bed with immersed horizontal tubes

BOSTON UNIVERSITY

COLLEGE OF ENGINEERING

Thesis

UNCERTAINTY QUANTIFICATION OF AN EFFECTIVE HEAT TRANSFER COEFFICIENT WITHIN A NUMERICAL MODEL OF A BUBBLING FLUIDIZED BED WITH IMMERSED HORIZONTAL TUBES

by

CHRISTOPHER MOULDER

B.S., Rensselaer Polytechnic Institute, 2010

Submitted in partial fulfillment of the

requirements for the degree of

Master of Science

2015

Approved by

First Reader _____

Emily Ryan, Ph.D.
Assistant Professor of Mechanical Engineering

Second Reader _____

Dan Cole, Ph.D.
Associate Professor of Mechanical Engineering

Third Reader _____

Pirooz Vakili, Ph.D.
Associate Professor of Mechanical Engineering
Associate Professor of Systems Engineering

UNCERTAINTY QUANTIFICATION OF AN EFFECTIVE HEAT TRANSFER COEFFICIENT WITHIN A NUMERICAL MODEL OF A BUBBLING FLUIDIZED BED WITH IMMERSED HORIZONTAL TUBES

CHRISTOPHER MOULDER

ABSTRACT

This study investigates sources of steady state computational uncertainty in an effective heat transfer coefficient (HTC) within a non-reacting bubbling fluidized bed with immersed horizontal heat-conducting tubes. The methodical evaluation of this variation, or Uncertainty Quantification (UQ), is a critical step in the experimental analysis process, and is particularly important when the values of input physical parameters are unknown or experimental data is sparse. While the concept applies broadly to all studies, this application investigates a 2D unit cell analogue of a bubbling fluidized bed designed for large-scale carbon capture applications. Without adequate characterization of simulation uncertainties in the HTC, bed operating characteristics, including the thermal efficiency, carbon capture efficiency, and sorbent half-life cannot be well understood. We focus on three primary parameters, solid-solid coefficient of restitution, solid-wall coefficient of restitution, and turbulence model, and consider how their influences vary at different bed solid fractions. This is accomplished via sensitivity analysis and the Bayesian Spline Smoothing (BSS) Analysis of Variance (ANOVA) framework. Results indicate that uncertainties approach 20% at high gas fractions, with the turbulence model accounting for 80% of this variation and the solid-solid coefficient of restitution accounting for the additional 20%.

Contents

List of Tables

List of Figures

List of Abbreviations

2D.....Two Dimensional

3D.....Three Dimensional

CEL..... Computational Energy Laboratory

CR-SS ..... Coefficient of Restitution Solid-Solid

CR-SW.....Coefficient of Restitution Solid-Wall

DOE .....Design of Experiments

GT .....Granular Temperature

HTC..... Heat Transfer Coefficient

MCMC .....Markov Chain Monte Carlo

MFIX.....Multiphase Flow with Interphase eXchanges

MGHPCC.....Massachusetts Green High Performance Computing Center

PDE.....Partial Differential Equation

SS .....Steady State

TFM .....Two-Fluid Model

Chapter 1

Introduction

Fluidized beds are used extensively in manufacturing and chemical processing systems due to their high mixing and reaction rates. However, the same physical processes that enable this behavior (e.g. high relative interphase velocities and numerous particle collisions) make accurate computational simulations exceptionally difficult. In addition, uncertainties in physical parameters that cannot be controlled and imperfect mathematical formulations of drag, turbulence, and other fluid phenomena add to the uncertainty of these computer simulations. In this study, we investigate the sources and magnitude of variation of an effective heat transfer coefficient (HTC) due to physical and mathematical unknowns within a non-reacting bubbling fluidized bed with immersed heat-conducting horizontal tubes for carbon capture applications. This analysis draws from uncertainty quantification principles to characterize the magnitude of uncertainty in the model output, as well as determine which parameters contribute most to this uncertainty.

While numerous carbon capture technologies are currently under study, dry supported amine sorbents are promising because of their reduced regeneration energy relative to aqueous systems [11] and the high tolerance of amine based sorbents to water vapor [27]. However, the heat transfer of supported amine based fluidized beds is particularly important due to their sensitivity to temperature. Sorbent CO_2 uptake can vary from high absorption to high desorption within 70˚C [40], requiring fine control of bed operating temperature. However, particle temperatures within a steady state bed can vary greatly at any individual location and time. Additionally, the bonding of CO_2 molecules to the

sorbents generates heat that must be removed [10]. Thus, the size, spacing, and temperature of cooling tubes are dependent on the ability of the fluid flow to efficiently transfer thermal energy. This interplay of heat generation, multiphase turbulent flow, and cooling tubes makes predicting the suspension temperature difficult, and therefore poses significant design challenges. Finally, many studies have seen that amine based sorbents can have a limited operating life due to absorption-desorption cycling [27,41]. This complex behavior generates significant model uncertainty that must be characterized by a controlled study.

Often, this analysis is in the form of uncertainty quantification (UQ) and sensitivity analysis (SA), where UQ is a statistical technique of quantifying how unknowns contribute to overall model uncertainty and SA quantifies how changes in model inputs influence the model output. Taken together, these tools allow one to identify important model parameters for further study or control and provide a benchmark to qualify the significance of analysis results. This study uses a Bayesian UQ framework called Bayesian Spline Smoothing Analysis of Variance (BSS-ANOVA) [23] to quantify the total uncertainty in the system and a main effects and interactions analysis to determine the most significant model parameters.

In general, the analysis of bubbling fluidized beds can be broken into three areas of research, hydrodynamics, thermodynamics, and reaction kinetics. The hydrodynamics question was addressed previously by Lane et al. who evaluated model uncertainty of bubbling frequency and phase fraction [19] using the BSS-ANOVA approach. The thermodynamics were somewhat addressed by Agrawal et al. who touched on several

factors affecting uncertainty in thermal diffusion and heat transfer [1]. However, his work only focused on uncertainties due to the model filtering process, see chapter 3.5, and the corrections required to back-out the unfiltered values. This work specifically addresses how uncertainty in model assumptions and physical unknowns affect heat transfer. Lastly, uncertainty due to reaction kinetics, especially as it pertains to carbon capture, remains to be evaluated.

The goal of this research is to increase the understanding of how turbulence model selection and particle coefficients of restitution, which are difficult to determine experimentally, affect the uncertainty of heat transfer within a fluidized bed. We seek to characterize this uncertainty within a statistically defensible framework by first constructing a representative 2D computer model of a bubbling fluidized bed with immersed heat-conducting horizontal tubes. Second, we develop a test matrix that appropriately captures the parameters of interest. Third, we apply a modern UQ framework that is well suited for categorical variables. Fourth, we analyze system sensitivity with a focus on easy-to-implement graphical methods. Finally, we present results as a function of bed gas fraction, a controllable characteristic, where at each gas fraction there is uncertainty due to the unknowns of turbulence model selection and the coefficients of restitution.

Chapter 2

System Definition

There are two primary components within a simplified, dry regenerable-sorbent carbon capture system: the absorber, or carbonation reactor, and the regenerator. See Figure 1. The absorber is where sorbents remove CO_2 from a carrier gas, and the regenerator removes the CO_2 from the sorbents and returns them back to the absorber to be used again. The removed CO_2 is then compressed and sequestered [22]. In this research, the expected carrier gas is flue exhaust from coal-fired power plants.

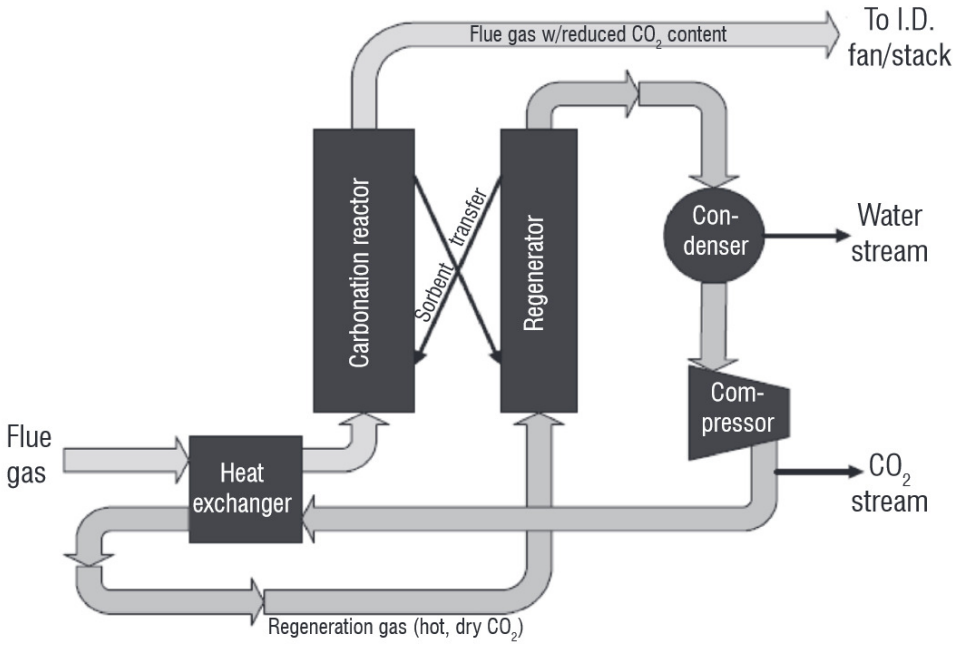

Figure 1 – Simplified carbon capture system [22]

We seek to model the absorber portion of the carbon capture system, where the actual carbon capture occurs within a fluidized bed. See Figure 2. Here, the fluidized bed is essentially a large vessel filled with amine-coated particles. Flue gas is then forced through the bottom of the vessel, causing it to mix with the particles and the CO_2 to be

stripped from the flow by the amine compounds. Consequently, the gas exiting the top of the bed has a much lower CO_2 content and is releasable to the outside environment.

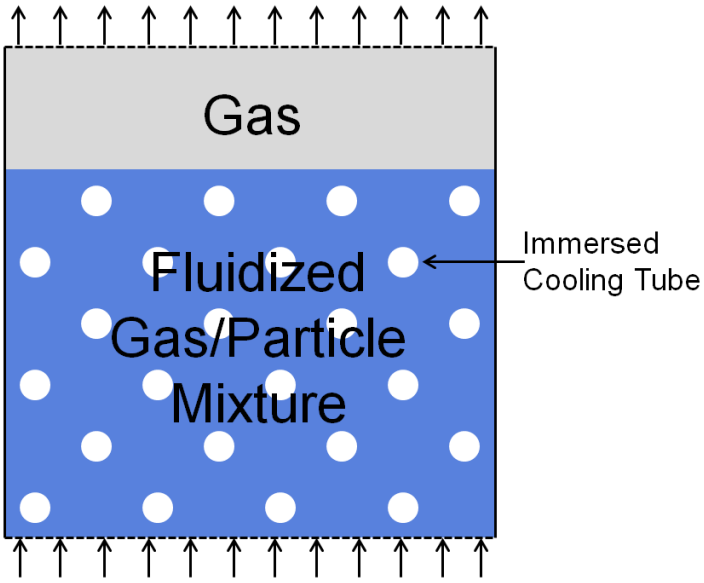

Figure 2 – Fluidized bed

Additionally, in the carbon capture scenario, the CO_2 absorption reaction generates heat that must be removed through cooling tubes. If the bed is allowed to heat up, the sorbents will release the CO_2 back into the flue gas stream.

Within fluidized beds, there are three main flow regimes, bubbling, turbulent, and fast fluidization, where the key factors include gas in-flow velocity and the solid volume fraction [9]. We primarily investigate the bubbling regime, where the bed maintains a definable interface with the exiting gas as in Figure 2. Here, gas flows from the bottom to the top of the bed by forming bubbles that force their way through the sorbents by creating large, moving cavities. However, as the gas velocity increases or the amount of solids decreases, the flow becomes more turbulent, the bubbles smaller, and the gas/solid mixture more homogeneous. This defines the turbulent regime.

Despite having a so-called turbulent regime, fluid turbulence is important in all flow regimes because it enhances momentum and heat transfer between the solid and gas phases. Even at high gas fractions where the thermal mass of solid particles is low, the particles can still have a significant effect on the gas phase turbulence [42]. Therefore, it is essential to quantify the effects of these turbulence models.

In addition to typical thermodynamic parameters, other key bed variables, especially as they relate to heat transfer, are the packed bed void fraction, particle coefficients of restitution, and the particle friction angles. The packed bed void fraction describes the minimum gas volume fraction that can occupy any region of the bed. This is defined by the particle geometry and is typically around 0.36 for spherical particles [30]. The coefficients of restitution, both solid-solid and solid-wall, define the fraction of kinetic energy that is conserved in collisions. Finally, the particle friction angles, both solid-solid and solid-wall, describe the angle between the normal and resultant forces at which shear failure occurs in collections of particles [3]. This has implications for particle clustering, particularly along the cooling tubes.

Chapter 3

Numerical Methods

In this study, the thermodynamics of a bubbling fluidized bed are analyzed using the Multiphase Flow with Interphase eXchanges (MFIX) [21] software package developed by the Department of Energy. MFIX was chosen because of its open source nature, allowing modification of the source code, particularly with respect to heat generation, and to maintain consistency with prior work within the Boston University Computational Energy Laboratory (CEL).

In addition, we use the Eulerian-Eulerian approach where both the solid and gas phases are modeled as their own impenetrable continua and physical properties are calculated along a defined mesh. In the case of one gas and one solid phase, this simplifies to the two-fluid model (TFM) described in this chapter. This is in contrast to the Eulerian-Lagrangian approach where the solid particles are discretely modeled. For relatively dispersed solid phases, the Eulerian-Lagrangian approach is viable as there are few particles to track. However, as the fraction of solids within the flow increases, Eulerian-Lagrangian simulations can become much more computationally intensive than Eulerian-Eulerian approaches [34]. Despite this, recent advances in discrete element modeling (DEM) within MFIX [28] would have enabled this study to be conducted with a Eulerian-Lagrangian approach. However, it has yet to go through the same rigorous verification and validation process as the TFM [14].

The statistical analysis of simulation results is conducted with the R software

packaged developed by The R Project for Statistical Computing [37], and the core BSS-ANOVA code was contributed by C. Storlie [31].

3.1 Governing Equations

The continuity and momentum equations for each phase are defined as

$$\frac{\partial}{\partial t}\left(\Phi_g \rho_g\right)+\nabla\cdot\left(\Phi_g \rho_g u_g\right)=0 \quad (1)$$

$$\frac{\partial}{\partial t}\left(\Phi_s \rho_s\right)+\nabla\cdot\left(\Phi_s \rho_s u_s\right)=0 \quad (2)$$

$$\frac{\partial}{\partial t}\left(\Phi_g \rho_g u_g\right)+\nabla\cdot\left(\Phi_g \rho_g u_g u_g\right)=\nabla\cdot\tau_g-\Phi_g\nabla P+\Phi_g \rho_g G-\beta\left(u_g-u_s\right) \quad (3)$$

$$\frac{\partial}{\partial t}\left(\Phi_s \rho_s u_s\right)+\nabla\cdot\left(\Phi_s \rho_s u_s u_s\right)=\nabla\cdot\tau_s-\Phi_s\nabla P+\Phi_s \rho_s G+\beta\left(u_g-u_s\right) \quad (4)$$

where subscripts g and s indicate the gas and solid phases respectively, Φ is the phase fraction, ρ is density, u is velocity, τ is stress, P is pressure, G is acceleration due to gravity, and β is the interphase momentum exchange coefficient.

Additionally, the conservation of internal energy for each phase is defined as

$$\frac{\partial}{\partial t}\Phi_g \rho_g Cp_g T_g+\nabla\cdot\left(\Phi_g \rho_g Cp_g T_g u_g\right)=\nabla\cdot\left(\Phi_g k_g \nabla T_g\right)+\gamma_{gs}\left(T_s-T_g\right) \quad (5)$$

$$\frac{\partial}{\partial t}\Phi_s \rho_s Cp_s T_s+\nabla\cdot\left(\Phi_s \rho_s Cp_s T_s u_s\right)=\nabla\cdot\left(\Phi_s k_s \nabla T_s\right)-\gamma_{gs}\left(T_s-T_g\right)+\Phi_s \rho_s Cp_s \dot{\Pi}_s \quad (6)$$

where Cp is specific heat, k is the thermal conductivity and $\dot{\Pi}_s$ is the heat generation of the solid phase due CO_2 capture.

3.2 Kinetic Theory

To satisfy all unknowns in the governing equations, it is necessary to define the amount of energy stored within the solid phase. Unlike in the Eulerian-Lagrangian framework, where the solid phase energy is physically apparent for each particle, the concept is more abstract in the TFM. The solid phase energy is instead defined as a

function of the root mean square of the solid phase velocity. The Kinetic Theory of Granular Flow (KTGF) quantifies this as the granular temperature (GT) [12], which is then used to calculate the solid phase pressure, solid phase viscosity, and the stress tensors. GT is expressed as

$$\frac{3}{2}\left[\frac{\partial}{\partial t}(\Phi_s \rho_s \Theta)\nabla\cdot(\Phi_s \rho_s \Theta)u_s\right] = \tau_s : \nabla u_s - \nabla\cdot q_\Theta - \gamma_\Theta + \Pi \qquad (7)$$

where Θ is granular temperature, q_Θ is diffusive flux of granular energy, γ_Θ is granular energy dissipation, and Π is the interphase exchange of granular energy.

Had this study not evaluated turbulence, an algebraic formulation for GT proposed by Syamlal [35] would have been much less computationally demanding; however, this formulation neglects diffusion and convection terms required by the turbulence models. To ensure consistent results, the full partial differential equation (PDE) was also used for the base simulation case with no turbulence.

The stress tensors are then given as

$$\tau_g = 2\mu_{gt}\left\{\frac{1}{2}\left[\nabla u_g + (\nabla u_g)^T\right] - \frac{1}{3}\nabla\cdot u_g I\right\} \qquad (8)$$

$$\tau_s = (-P_s + \upsilon\mu_b\nabla\cdot u_s)\bar{I} + 2\mu_s\left\{D_s - \frac{1}{3}\nabla\cdot u_s I\right\} \qquad (9)$$

$$D_s = \frac{1}{2}\left[\nabla u_s + (\nabla u_s)^T\right] \qquad (10)$$

where μ_{gt} is turbulent viscosity, $\bar{I}$ is a unit tensor, P is pressure, υ is the coefficient of restitution, and D is rate of strain. As a note, the solids-stress tensor is not valid at very low solid fractions; however, it should be acceptable throughout the entire simulation regime, as we do not analyze scenarios below a solid fraction, Φ_s, of 0.05. Additionally, it

has been shown that filtered TFM simulations are relatively insensitive to the gas phase viscosity [2], so we set μ_{gt} equal to the molecular value.

3.3 Drag

It is necessary to model particle drag to allow for momentum exchange between the solid and gas phases due to velocity variations between the phases and buoyancy effects due to pressure gradients [36]. Three particle drag, or interphase momentum exchange, models are available within the MFIX software package. These are the Gidaspow, Syamlal-O'Brien, and Wen-Yu models [6]. In this study, we use the Wen-Yu model as it was previously determined by Lane et al. to be most applicable to this application [19]. Here, the interphase momentum exchange coefficient is defined as

$$\beta = \frac{3}{4}\frac{\rho_g \Phi_g \Phi_s}{d_s} C_D \left| u_g - u_s \right| \Phi_g^{-2.65} \qquad (11)$$

where the Coefficient of Drag, C_D, is defined as

$$C_D = \begin{cases} \frac{24}{\Phi_g \, \mathrm{Re}_s}\left[1 + 0.15\left(\Phi_g \, \mathrm{Re}_s\right)^{0.687}\right] & \mathrm{Re}_s < 1000 \\ 0.44 & \mathrm{Re}_s > 1000 \end{cases} \qquad (12)$$

where Re_s is the Reynolds number derived from the solid-phase particle diameter and the slip velocity.

3.4 Turbulence

To evaluate the effect of turbulence model selection on simulation uncertainty, three levels of turbulence were chosen for analysis: no turbulence or laminar, a standard K-Epsilon model [12], and the Simonin turbulence model [4]. The Ahmadi model [8] was also considered; however, model stability and convergence speed were significantly reduced in our simulations.

The standard K-Epsilon turbulence formulation plus interphase exchange terms is presented below, but can be more simply described as: transient + convection = diffusion + production + destruction (of turbulent kinetic energy, k, or dissipation of turbulent energy, ε).

Gas Phase Turbulence

$$\Phi_g \rho_g \left[\frac{\partial k_g}{\partial t} + U_{g,j} \frac{\partial k_g}{\partial x_j} \right] = \frac{\partial}{\partial x_i} \left(\Phi_g \frac{u_g^t}{\sigma_k} \frac{\partial k_g}{\partial x_i} \right) + \Phi_g \tau_{g,i,j} \frac{\partial U_i}{\partial x_j} + \prod_{k1} - \Phi_g \rho_g \varepsilon_g \qquad (13)$$

$$\Phi_g \rho_g \left[\frac{\partial \varepsilon_g}{\partial t} + U_{g,j} \frac{\partial \varepsilon_g}{\partial x_j} \right] = \frac{\partial}{\partial x_i} \left(\Phi_g \frac{u_g^t}{\sigma_\varepsilon} \frac{\partial \varepsilon_g}{\partial x_i} \right) + \Phi_g \frac{\varepsilon g}{k_g} \left(C_{g,\varepsilon} \tau_{g,i,j} \frac{\partial U_i}{\partial x_j} - \rho_g C_{2,\varepsilon} \varepsilon_g \right) + \prod_{\varepsilon 1} \qquad (14)$$

Solid Phase Turbulence

$$\Phi_s \rho_s \left[\frac{\partial \Theta_s}{\partial t} + U_{s,j} \frac{\partial \Theta_s}{\partial x_j} \right] = \frac{\partial}{\partial x_i} \left(\Phi_s \rho_s \kappa_s \frac{\partial \Theta_s}{\partial x_i} \right) + \Phi_s \rho_s \tau_{s,i,j} \frac{\partial U_{s,i}}{\partial x_j} + \prod_{k2} - \Phi_s \rho_s \varepsilon_s \qquad (15)$$

where U is average phase velocity, μ is turbulent eddy viscosity, σ is the viscous stress tensor, τ is Reynolds stress, Π are turbulent exchange terms, C are fixed model coefficients, Θ_s is the granular temperature, and κ_s is the granular conductivity. In the K-Epsilon model, the turbulent interphase exchange terms are equal to zero. However, in the Simonin model they are defined as

$$\prod_{k1} = \beta (k_{12} - 2k_1) \qquad (16)$$

$$\prod_{\varepsilon 1} = C_{3\varepsilon} (\varepsilon_1 / k_1) \prod_{k1} \qquad (17)$$

$$\prod_{k2} = \beta (k_{12} - 3\Theta_s) \qquad (18)$$

$$k_{12} = \frac{\eta_t}{1 + (1 + X_{21}) \eta_t} (2k_1 + 3X_{21} \Theta_s) \qquad (19)$$

where k_{12} is the cross-correlation of gas and solid phase fluctuating velocities, η_t is the ratio between the Lagrangian integral time scale and the particle relaxation time, and X_{21} is the volume weighted solid-gas density ratio. It is these additional terms that allow the turbulent energy within the solid to interact with the gas phase.

3.5 Model Filtering

Model filtering is the process of converting fine-grid simulations, such as those modeled here in MFIX, to coarse-grid surrogates that capture the macro scale behavior of the system. These coarse-grid surrogates can then be approximated by computationally efficient statistical models, such as the BSS-ANOVA. In this research, the ultimate goal is to be able to combine many of the coarse-grid filtered models together to construct a full-scale model of a fluidized bed that accurately predicts the system-level behavior. Despite the computational benefits, the filtering process can introduce its own set of biases and uncertainties [1]; however, the analysis of this uncertainty is left to future work.

The filtering process used in this work is simply the average of all cells within the simulation mesh or

$$X_{filtered} = \frac{1}{96 \cdot 96} \sum_{i=1}^{96} \sum_{j=1}^{96} X_{i,j} \qquad (20)$$

where X is the parameter of interest, such as the gas temperature, T_g, and the model mesh size is 96 x 96 cells.

Chapter 4

Computational Setup

We model a simplified surrogate of bubbling fluidized bed for use in carbon capture applications. The two primary simplifying assumptions are that a 2D analysis and a filter size of one characteristic length provide reasonable correlation to the full-scale, 3D scenarios. The 2D/3D question has been addressed by Igci et al. for filtered sub-grid modeling applications [16] and Li et al. [38] for full system simulations, e.g. bench-scale testing. While these studies address interphase momentum transport and bubble dynamics, and not heat transfer specifically, we do not expect the results to be wholly dissimilar. Recent work by Lane et al. has also shown that a filter size of one characteristic length, the smallest self-consistent repeating structure within the bed (see Figure 3: Right) results in very similar steady state suspension temperatures [18]. This most likely also validates results for bed heat transfer.

The final geometry is presented in Figure 3: Left, where the outer walls have cyclic boundary conditions and the immersed horizontal tubes have a no-slip boundary condition for the gas phase and the partial slip Johnson-Jackson boundary condition [17] for the solid phase. The Johnson-Jackson boundary condition is necessary, as the flow behavior around the tubes will vary significantly depending on the local solid fraction – at high solid fractions, frictional shear forces between clustered particles are important, while at low solid fractions, collisions are brief and mostly involve only normal reaction forces. Additionally, the dominant flow moves in the y-direction from the bottom of the figure to the top.

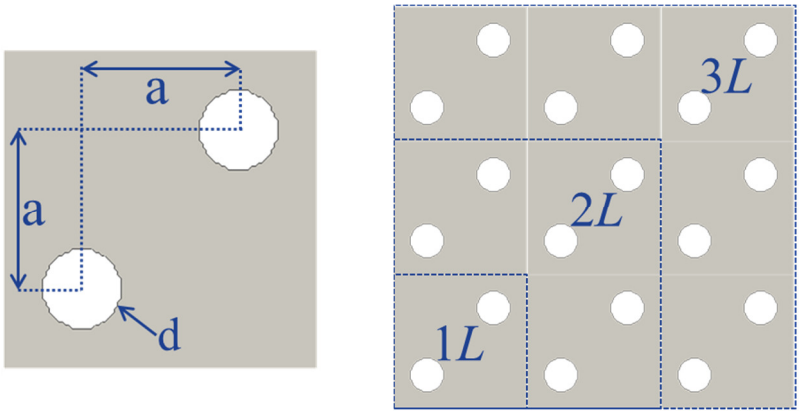

Figure 3 – Example geometry (left). Possible filter sizes (right), where L is the characteristic length

The HTC analyzed in this research is defined in Equations 21–24 as

$$h = \frac{Q}{dT} \tag{21}$$

$$Q = \left(1 - \Phi_g\right)\rho_s Cp_s \dot{\Pi}_s \tag{22}$$

$$dT = T_{wall} - \tilde{T} \tag{23}$$

$$\tilde{T} = \frac{\Phi_g \rho_g Cp_g T_g + \left(1 - \Phi_g\right)\rho_s Cp_s T_s}{\Phi_g \rho_g Cp_g + \left(1 - \Phi_g\right)\rho_s Cp_s} \tag{24}$$

where the effective bed temperature, $\tilde{T}$, is simply a scaled average of the solid and gas phase temperatures. Here, we have chosen to scale by phase mass and specific heat to better capture the effect of internal energy.

Due to the way MFIX implements heat generation, the heat flux does not have a length scale. Therefore, our HTC has units of W/m^{3}K instead of the standard W/m^{2}K. Despite the difference, we believe this definition appropriately captures the scale of thermal energy transfer within the system and allows for comparison across the parameters of this study. We have not specifically validated bed temperatures, but we believe the results are

accurate due to qualitative evaluation of the system and the magnitude of observed responses.

Physical and thermodynamic constants are presented in Table 1. Additionally, the horizontal tubes are held at a constant temperature of 293K, and the solid phase has a heat generation term, $\dot{\Pi}_s$, of 1K/s. Here, the absolute magnitude of heat generation is not of particular importance because the value cancels out in the calculation of the HTC. More specifically, as heat generation increases, T_s and T_g increase in a corresponding manner to result in a higher steady state bed temperature. This higher bed temperature then cancels out with the greater heat flux in Equation 21 to yield a similar HTC.

Table 1: Model geometry and physical properties

Parameter	Value	Parameter	Value
Bed		Conductivity (W/m·K)	0.024
Width (m)	0.12	Specific Heat (J/kg·K)	1150
Height (m)	0.12	Initial Temperature (K)	293
Mesh Size	96x96	Solid Phase	
Tube		Density (kg/cm$^{3)}$	441
Number of Tubes	2	Conductivity (W/m·K)	0.2
Diameter (m)	0.015	Specific Heat (J/kg·K)	1000
Spacing (cm)	0.06	Heat Generation (K/s)	1.0
Gas Phase		Max Packing Factor	0.36
Density (g/cm^3)	1.3	Particle Diameter (m)	150E-6
Viscosity (kg/m·s)	18E-6	Initial Temperature (K)	293

To induce bed fluidization, a differential pressure gradient, ΔP, is applied along the vertical direction of the geometry as given by

$$\Delta P = \psi\left(\Phi_g \rho_g + \left(1 - \Phi_g\right)\rho_s\right)Gl \qquad (25)$$

where the minimum bed fluidization differential pressure is given by $\psi=1$ and l is the bed width. Thus, as ψ increases, the upward fluid velocity increases. Additionally, to maintain comparable fluid flow across all solid fractions, ΔP is allowed to vary for each simulation. We selected a ψ of 1.3 to ensure that the average flow direction is primarily upwards, in line with typical bed operation. Additionally, this improved model convergence by reducing the occurrence of reverse flow.

Finally, to ensure consistent results, all models were simulated to 10 seconds of real-time steady state behavior, where steady state is defined as 99.3% of the predicted steady state suspension temperature given by an exponential fit.

All simulations were conducted at the Massachusetts Green High Performance Computing Center (MGHPCC), each using 4 parallel cores of an Intel Xeon E5-2680 CPU. Simulation times ranged from 4–10 days depending on the solid fraction and turbulence model. Data was sampled at 20 Hz, which proved more than adequate to capture the steady state variation within the simulations.

Chapter 5

Statistical Analysis

5.1 Selected Parameters

The impact of turbulence model selection is particularly important to this study because it not only holds potential to increase model uncertainty, but also because modeling turbulence is much more computationally demanding. Given that we do not know the correct turbulence model, multiple models must be investigated to determine the significance of the selection on heat transfer results. Three models are analyzed: a base case with no turbulence (laminar), a standard K-Epsilon model, and the Simonin model. While the K-Epsilon and Simonin models are of nearly identical form, the key benefit of the Simonin formulation is additional terms that allow turbulent interphase momentum exchange. We expect little difference between all three models at low bed gas fractions, where the flow is dominated by solid-solid collisions, but increasing discrepancy at higher gas fractions.

Consistent with work by Lane et al., the impact of the coefficients of restitution for solid-solid and solid-wall interactions is also analyzed. These coefficients are important because the true values are difficult to determine experimentally and are often unknown. The friction angles are held constant at 28 degrees, and the packed bed void fraction is held constant at 0.36 because these values can be readily confirmed experimentally. A summary of all evaluated model parameters and their values is presented in Table 2.

Table 2: Model parameters

Model Inputs (x_i)		Distribution
x_1	Gas Fraction	~U(0.4,0.538,0.675,0.813,0.95)
Model Parameters (θ_i)		
θ_1	Coefficient of restitution. S-S	~N(0.9, .033)
θ_2	Coefficient of restitution S-W	~N(0.9,0.033)
θ_3	Turbulence Model	~U(Laminar, K-Epsilon, Simonin)
Model Outputs (y_i)		
y_1	Heat Transfer Coefficient	---

5.2 Sampling

Given the computing resources available for the study and the length of time each simulation requires, it was only feasible to complete 90 simulations. Therefore, it was important to select the test points in a methodical fashion. A variety of test matrices were evaluated, including Latin Hypercube Sampling (LHS) [24], classical Design of Experiments (DOE) setups with evenly spaced test points, and a pure Monte Carlo [39]. However, LHS has several benefits for this application.

Instead of randomly selected test points within a design space, LHS subdivides the sample range into regions of equal probably, or bins, then randomly picks points within each of those bins. Through this process, the experimenter has much greater ability to ensure that the entire test range is adequately sampled. However, this is not the only benefit. Due to the limited number of test points that may be selected within a specific subset of the design space, it is possible create correlation between independent variables if samples are not chosen carefully. If this occurs, it may be impossible to ascertain which input variable induces a change in the dependent output parameter. LHS specifically

addresses this by minimizing pairwise correlations and maximizing the distance between points. Finally, the BSS-ANOVA method described in chapter 5.3 allows sharing of model behavior between categorical parameters. This means that peaks, troughs, and other identifiable features in the output of one categorical parameter can reveal themselves in another, despite not having any data points in that region. The net effect of this is increased test power, or the ability to ascertain a change in output, by selecting test points that do not lie on top of each other between categorical inputs. This is not easily achieved in a standard DOE matrix such as face-centered cubic or body-centered cubic design.

A Monte Carlo approach is vulnerable to several of the issues discussed above: it does not control for correlations and it can over-sample or under-sample test regions. Conversely, it is much more efficient at generating test matrices with large numbers of parameters and samples. Despite this, research indicates that these risks are mostly unfounded when there are a large number of model parameters and samples [15]. However, as is the case with this study, only a small number of model parameters are investigated and resources only allow for 90 simulations. Thus, the LHS approach was selected as the most appropriate method for this study.

Once the test matrix was generated, it was necessary to validate the sample correlations and general space filling quality. Figure 4 presents the results of the correlation analysis for the samples in this study, where COR-SS is the Coefficient of Restitution for Solid-Solid interactions, COR–SW is the Coefficient of Restitution for Solid-Wall interactions, Turb is turbulence model, and Phis is the solid fraction.

	COR-SS	COR-SW	Turb
COR-SW	-0.049		
	0.650		
Turb	-0.073	0.075	
	0.495	0.483	
Phis	-0.002	-0.080	0.000
	0.986	0.451	1.000

Figure 4 – Linear correlation of model parameters in study. Top row is correlation, bottom row is statistical p-value

The p-values, or probability due to random chance, of the correlations are all large, >> 0.05, therefore, there is no evidence that a linear relationship exists among the model parameters. Thus, it is unlikely that we will not be able to determine which predictor causes a change in the model output due to sample correlation. The next step is to visually confirm that there is no correlation among parameters, as in Figure 5.

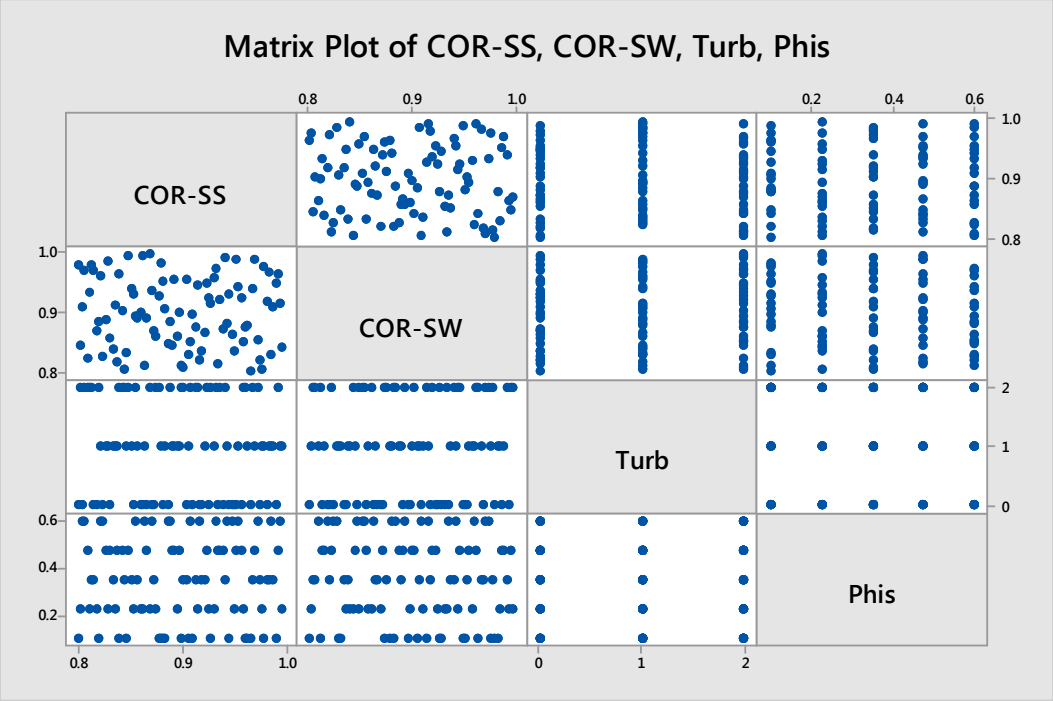

Figure 5 – Graphical view of model parameter correlation

Finally, as shown in Figure 6, a histogram of the test points verifies that the entire test range is evenly sampled.

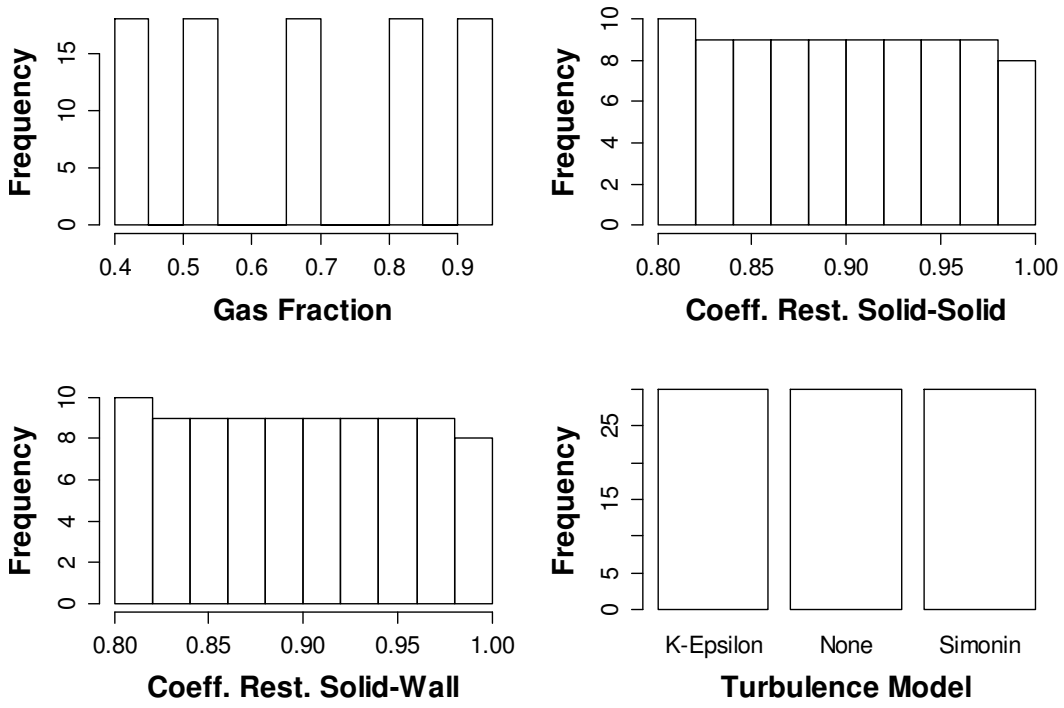

Figure 6 – Histogram of Latin hypercube sampled test matrix

5.3 BSS-ANOVA

The BSS-ANOVA process is essentially an additive model composed of main effects and interactions represented as zero-mean Gaussian processes. However, it has a number of important benefits over other Bayesian curve fitting methods. First, a special covariance matrix allows categorical predictors. Second, categories can gain "strength" for other categories [32]. Finally, model calibration, or the correction of simulation bias with experimental data, is easily integrated into the model. Additionally, because it is an additive model with variable selection, it is relatively easy to discern the importance of

each model parameter, unlike some methods that include all interaction terms or whose descriptors combine multiple main effects or interactions together [23].

As an additional note, the model efficiency is greatly enhanced due to stochastic variable selection and not inverting large matrices within the Markov Chain Monte Carlo (MCMC) process. However, the specifics of this are left to Storlie et al. as they are less crucial to explaining the concept of BSS-ANOVA and how it applies to calculating model uncertainty [32].

In its most basic form BSS-ANOVA model is represented as

$$y_n = \eta(x_n, \theta) + \delta(x_n) + \varepsilon_n \quad (26)$$

where y is the experimental HTC data that we wish to model, $\eta(x_n, \theta)$ is the statistical model of y based on the MFIX simulation results, also known as the emulator, x_n are the model inputs (gas fraction), θ the model parameters (coefficient of restitution and turbulence model), $\delta(x_n)$ a discrepancy function to correct for MFIX model bias, and ε_n the measurement error. It is important to recognize that $\eta(x_n, \theta)$ is not merely a computationally efficient representation of the MFIX model, but probabilistically accounts for the steady state variation of the system, physical parameter uncertainties, and categorical model assumptions. For simplicity, we substitute ω as a vector of the model inputs and parameters. The emulator can then be expressed as

$$\eta(\omega) = \alpha_0 + \sum_{n=1}^{N} \eta_n(\omega_n) + \sum_{n<n'}^{N} \eta_{n,n'}(\omega_n, \omega_{n'}) + \cdots \quad (27)$$

where N is the sum of all linear transformations of the model inputs and parameters, N=P+Q, α_0 is an intercept ~ $N(0, \varsigma_0^2)$, η_n the main effects ~ $GP(0, \varsigma_n^2 K_1)$, and $\eta_{n,n'}$ the

interaction terms ~ GP(0, $\varsigma_{n,n'}^2$ K_2). Additionally, for categorical terms, $\eta_n(\omega_n)$ ~ GP(0, λ_n^2 K_d).

The covariance function of the main effects is defined as

$$K_1(u,u') = B_1(u)B_1(u') + B_2(u)B_2(u') - \frac{1}{24}B_4(|u-u'|) \quad (28)$$

where the B_x terms are the x-th Bernoulli polynomials. Interaction covariance terms are simply the products of the main effect covariance functions as shown below.

$$K_2((u,v),(u',v')) = K_1(u,u')K_1(v,v') \quad (29)$$

For categorical terms, covariance is defined as

$$K_d(u,u') = \frac{G_n - 1}{G_n} I(u = u') - \frac{1}{G_n} I(u \neq u') \quad (30)$$

where G_n is the number of discrete categorical terms and I is the indicator function [33]. Interactions between categorical and continuous terms are again just the product of the main effect terms as described in Equation 29.

The power of the BSS-ANOVA method is more apparent when each functional component is represented as an orthogonal basis expansion as in

$$\eta_n(\omega_n) = \sum_{k=1}^{\infty} \alpha_{n,k}\phi_k(\omega_n) \quad (31)$$

for the continuous terms and

$$\eta_n(\omega_n) = \sum_{k=1}^{G_n} \alpha_{n,k}\left[\frac{G_n - 1}{G_n} I(\omega_n = k) - \frac{1}{G_n} I(\omega_n \neq k)\right] \quad (32)$$

for the categorical terms. Here, ϕ_k is the k-th eigenfunction of the Karhunen-Loéve expansion [20]. In other words, the influence of each model component is described by the sum of a series of physically describable curves. Additionally, $\alpha_{n,k}$ ~ N(0, ς_n^2). In the

case of categorical parameters, the prior $\alpha_{n,k}$ serves an important purpose of penalizing resulting models that stray from the categorical average. Thus, because levels are promoted to behave similarly, missing data can be managed via the influence of categories where data does exist. While this behavior does not extend well to step functions, it does perform well for the smooth, continuous behavior under study.

The next step in the BSS-ANOVA process is to generate the discrepancy function $\delta(x_n)$ to correct for model bias between the MFIX simulation data and experimental data. This itself is an additive Gaussian process generated in exactly the same manner as the emulator, $\eta(\omega)$. However, this study does not have experimental data to validate against, so the details are left to Storlie et al.

Finally, a Gibb's MCMC sampler is used to generate plausible emulator outcomes that match the MFIX data, as shown by the Emulator Reals in Figure 7. The sampler input distributions are given in Table 2. At this point, one could use the posterior distributions of the MCMC samples to determine the model parameter values that are most likely to result in the observed experimental data.

Thus, the BSS-ANOVA process captures uncertainty due to observation error, the model fit itself, and by extension of its application, physical and mathematical model uncertainty. Therefore, it is an extremely powerful tool when used to quantify experimental unknowns.

Chapter 6

Results

Of the 90 attempted model simulations, 84 completed, 1 did not converge within the allotted computing time, and 5 failed to converge. The 5 failures are grouped at high solid fractions, which is expected given that large solid fractions promote particle packing, which can be numerically difficult to solve [5].

As seen in Figure 7, the HTC is presented as a function of bed gas fraction (a controllable parameter). At each gas fraction, uncertainty in the HTC due to turbulence model selection and the coefficients of restitution is given by the red 95% credible bounds. Visually, we see that the HTC starts at approximately 5750 (W/m^3K) at $\Phi_g = 0.4$, and then steadily decreases to 5250 (W/m^3K) by $\Phi_g = 0.8$. However, at that point, the results of the turbulence models diverge, with the K-Epsilon model dropping to 4000 (W/m^3K), while the Simonin and laminar models only decrease to 4750 (W/m^3K). This divergence contributes greatly to the model uncertainty at high gas fractions. However, the general downwards trend is expected as the conductivity of the gas is much less than that of the solid.

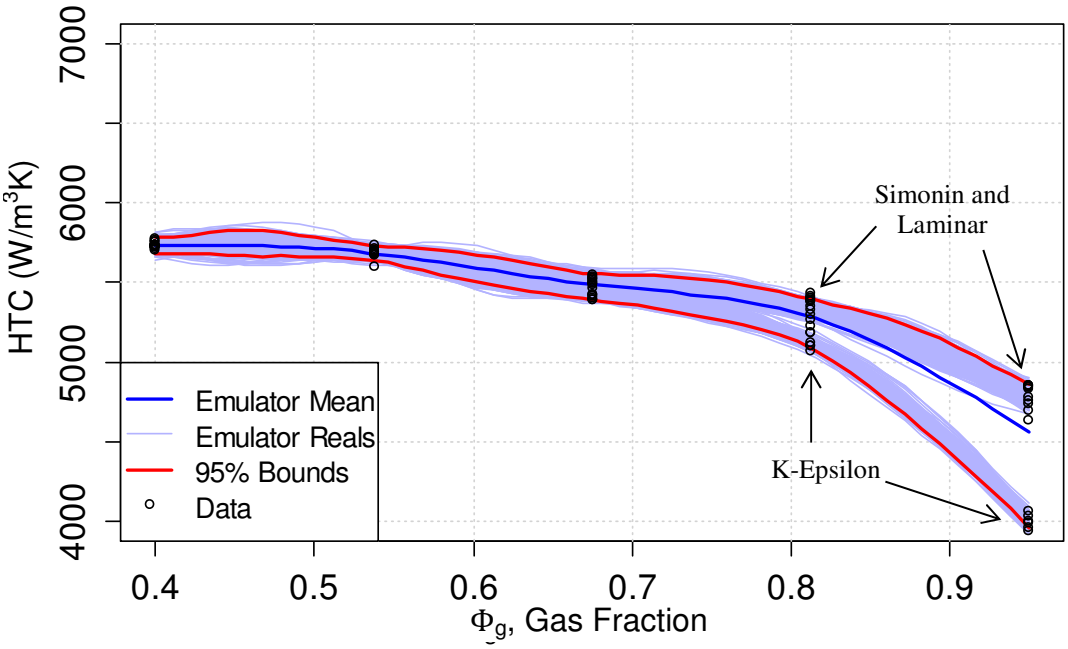

Figure 7 – Emulator output. Heat transfer coefficient as a function of gas fraction.

6.1 Uncertainty

The divergence of turbulence models is particularly interesting because the laminar model provides similar results to that of the Simonin model. Review of the steady state particle distributions in Figure 8 shows that the Simon and laminar models have greater particle clustering, particularly along the tube walls. This increased proximity to the cooling tubes should promote heat transfer.

Previous studies have shown that at fine grid sizes the KTGF, our laminar model, can predict proper particle clustering [14]. If particle clustering is the primary contributor to the difference in the HTC, and our grid size is adequate, then it is plausible that the Simonin and laminar models could yield similar HTCs. Thus, the difference in results is likely due to an improper energy balance in the K-Epsilon model as a result of its limitations on interphase turbulent energy exchange.

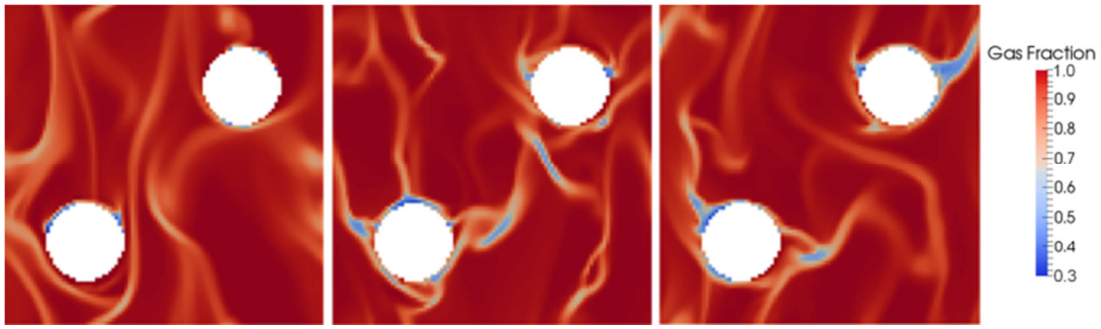

K-Epsilon Laminar Simonin

Figure 8 – Particle clustering at Φ_g=0.95. The K-Epsilon model shows less clustering, particularly along the tube walls.

Table 3 shows that model uncertainty is approximately 2% at low gas fractions and 20% at high gas fractions where the turbulence models diverge.

Table 3: Model uncertainty given by 95% credible bands

Φg, Gas Fraction	Total Uncertainty (%)
0.400	1.9
0.538	1.7
0.675	3.0
0.813	5.9
0.950	20.4

6.2 Sensitivity

The sensitivity of the model output can be evaluated by a large number of methods. One common global sensitivity tool is Sobol indices, which calculate the variance in model output assignable to specific input parameters [29]. An additional method that has been adapted to categorical variables is the calculation of the Total Variance Index as described by Saltelli et al. [25]. However, simpler methods can be equally effectively, even if not as statistically rigorous. The most common technique is the graphical representation of the main effects and interactions as in Figure 9. Here, the mean value of

the model output is plotted as a function of gas fraction while all but one parameter is held constant.

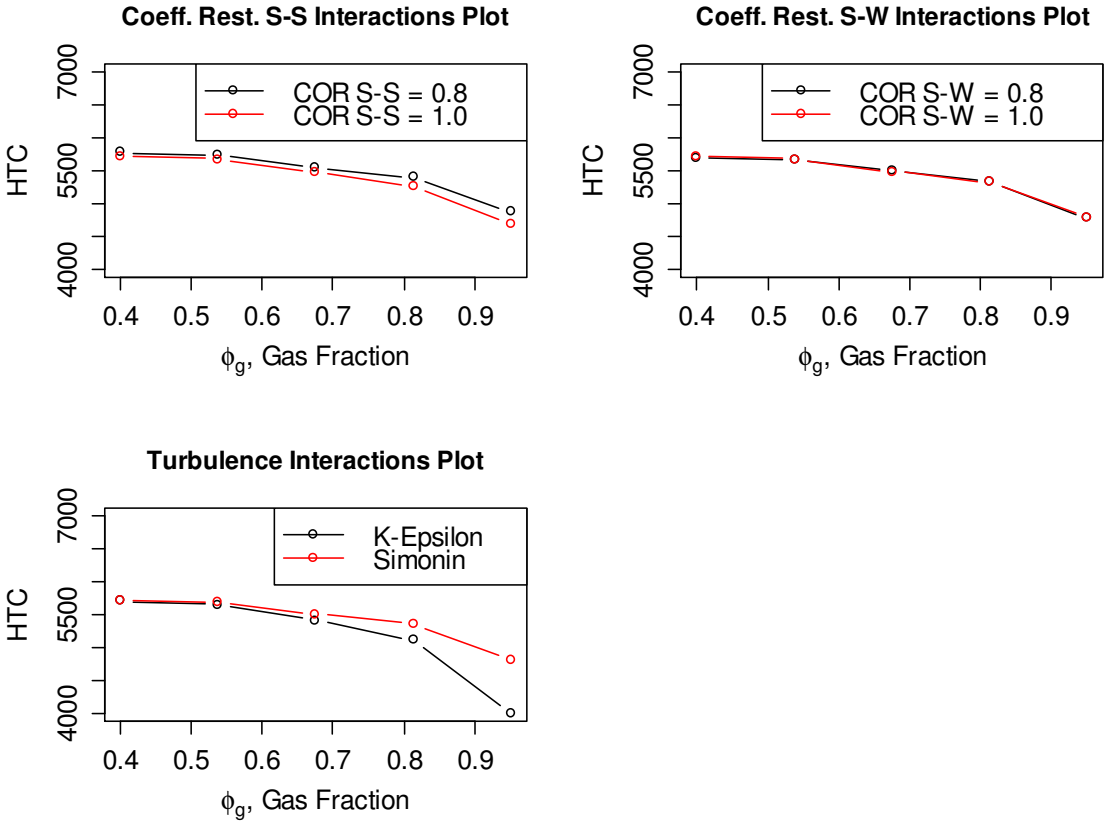

Figure 9 – Model interaction plots

It is clear that the solid-wall coefficient of restitution is nearly inconsequential to the model result. However, the solid-solid coefficient of restitution does have a measureable impact that grows greater with gas fraction. Lastly, the turbulence model has the greatest effect. This same data can also be plotted as the delta given by the maximum and minimum parameter levels scaled by the total variation of all parameters, such as in Figure 10. While this does not capture higher order interactions evaluated in other methods, the results echo what is apparent from the interaction plots.

That is, relative to the total variance, the importance of turbulence model is small at low gas fractions and high at high gas fractions, and the solid-solid coefficient of restitution is important at low gas functions, but much less so at high gas fractions. Both results are consistent with the underlying kinetic theory. At low gas fractions, due to the volume occupied by the solid phase, many more particle collisions occur. Therefore, the flow is dominated by particle kinetics, not the turbulent gas phase. Conversely, at high gas fractions, much less volume is occupied by the solid phase. Thus, the flow behavior is dominated by the gas phase and the turbulence model will be more important.

Additionally, it is important to consider the significance of variance relative to the entire simulation. While parameters may show an influence on average bed performance, it is essential to consider the significance of that influence relative to the steady state (SS) variation. As seen in Figure 10, the dashed line represents the steady state variation within the system. If one were interested in preventing a minimum or maximum heat transfer rate, it is clear that the steady state variation can be much more significant than some parameters.

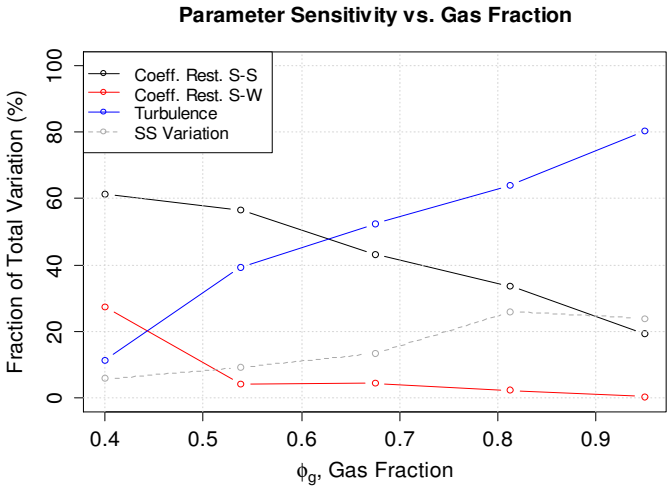

Figure 10 – Fraction of variance attributable to model main effects

Chapter 7

Conclusions

The BSS-ANOVA framework discussed in this paper was applied to a complex CFD problem. The results of this analysis were then used to quantify the uncertainty of an effective heat transfer coefficient within a bubbling fluidized bed with immersed horizontal heat-conducting tubes. In addition, a basic sensitivity analysis was performed. The results indicate uncertainty in model results of approximately 20% at high gas fractions and as low as 2% at low gas fractions, independent of unknown model biases. In addition, the choice of turbulence model is a significant factor at high gas fractions, explaining approximately 80% of the uncertainty, and the solid-wall coefficient of restitution is the greatest contributor to uncertainty at low gas fractions, explaining 60% of the uncertainty. Additionally, it was seen that while the Simonin and the laminar models yielded similar results, the K-Epsilon model diverged significantly from the other two models at high gas fractions. Future fluidized bed analyses should take note that including turbulence effects alone is not sufficient. Care must be taken to select an appropriate model, as results have significant implications for bed CO_2 absorption capability and cooling system design.

In addition to determining the specific characteristics of the K-Epsilon turbulence model that cause decreased particle clustering at high gas fractions, future work should also evaluate the validity of alternative filtering processes. Specifically, how calculating heat transfer across the entire averaged domain compares to calculating the heat transfer at each mesh location and then averaging across the entire domain. More broadly, work

up to this point has focused on the uncertainties of small-scale models. A full-scale fluidized bed model constructed from the coarse-grid filtered models is sure to have its own uncertainties. These uncertainties should also be evaluated in a controlled and statistically defensible manner.

Appendix 1

Table 4: Summary of simulation results

Simulation	Gas Fraction	Turbulence Model	COR S-S	COR S-W	HTC (W/m^3K)
1	0.400	K-Epsilon	0.822	0.959	5756.9
2	0.400	K-Epsilon	0.864	0.809	5719.7
3	0.400	K-Epsilon	0.944	0.880	5718.1
4	0.400	K-Epsilon	0.955	0.942	5726.3
5	0.400	K-Epsilon	0.986	0.827	5730.6
6	0.400	K-Epsilon	0.995	0.915	5751.8
7	0.400	Laminar	0.804	0.908	5766.7
8	0.400	Laminar	0.824	0.824	5773.8
9	0.400	Laminar	0.871	0.935	5729.3
10	0.400	Laminar	0.886	0.846	5728.6
11	0.400	Laminar	0.917	0.818	5728.8
12	0.400	Laminar	0.948	0.862	5730.6
13	0.400	Simonin	0.807	0.970	Did Not Converge
14	0.400	Simonin	0.855	0.893	5705.8
15	0.400	Simonin	0.889	0.884	5719.2
16	0.400	Simonin	0.908	0.851	Did Not Converge
17	0.400	Simonin	0.933	0.973	5718.1
18	0.400	Simonin	0.973	0.853	5715.7
19	0.538	K-Epsilon	0.827	0.886	5688.5
20	0.538	K-Epsilon	0.838	0.815	5688.3
21	0.538	K-Epsilon	0.891	0.844	5601.8
22	0.538	K-Epsilon	0.893	0.955	5684.1
23	0.538	K-Epsilon	0.897	0.900	5687.6
24	0.538	K-Epsilon	0.970	0.988	5674.4
25	0.538	Laminar	0.831	0.855	5694.4
26	0.538	Laminar	0.866	0.891	5694.1
27	0.538	Laminar	0.935	0.813	5686.3
28	0.538	Laminar	0.939	0.871	5683.2
29	0.538	Laminar	0.953	0.986	5684.7
30	0.538	Laminar	0.957	0.922	5683.3
31	0.538	Simonin	0.809	0.822	5712.3
32	0.538	Simonin	0.842	0.902	5702.6
33	0.538	Simonin	0.849	0.995	5736.7
34	0.538	Simonin	0.924	0.946	5694.9
35	0.538	Simonin	0.937	0.920	Did Not Converge
36	0.538	Simonin	0.993	0.962	5674.0
37	0.675	K-Epsilon	0.833	0.838	5422.7
38	0.675	K-Epsilon	0.851	0.937	5404.9
39	0.675	K-Epsilon	0.858	0.889	5424.0

40	0.675	K-Epsilon	0.922	0.864	5412.8
41	0.675	K-Epsilon	0.984	0.966	5392.3
42	0.675	K-Epsilon	0.988	0.906	5394.1
43	0.675	Laminar	0.815	0.968	5495.0
44	0.675	Laminar	0.873	0.866	5542.2
45	0.675	Laminar	0.904	0.953	5539.8
46	0.675	Laminar	0.920	0.833	5523.4
47	0.675	Laminar	0.975	0.820	5509.1
48	0.675	Laminar	0.982	0.917	5519.3
49	0.675	Simonin	0.813	0.977	Did Not Converge
50	0.675	Simonin	0.844	0.804	Did Not Converge
51	0.675	Simonin	0.902	0.807	5528.9
52	0.675	Simonin	0.913	0.875	5463.8
53	0.675	Simonin	0.942	0.990	5479.7
54	0.675	Simonin	0.968	0.939	5490.2
55	0.813	K-Epsilon	0.829	0.984	5183.3
56	0.813	K-Epsilon	0.835	0.911	5125.2
57	0.813	K-Epsilon	0.895	0.858	5186.5
58	0.813	K-Epsilon	0.931	0.957	5102.8
59	0.813	K-Epsilon	0.977	0.802	5098.8
60	0.813	K-Epsilon	0.997	0.840	5064.1
61	0.813	Laminar	0.818	0.869	5377.6
62	0.813	Laminar	0.853	0.931	5381.7
63	0.813	Laminar	0.860	0.897	5223.8
64	0.813	Laminar	0.862	0.993	5394.8
65	0.813	Laminar	0.926	0.924	5428.3
66	0.813	Laminar	0.951	0.835	5347.0
67	0.813	Simonin	0.802	0.842	5399.4
68	0.813	Simonin	0.811	0.933	5415.7
69	0.813	Simonin	0.869	0.997	5267.6
70	0.813	Simonin	0.875	0.860	5401.0
71	0.813	Simonin	0.915	0.944	5331.6
72	0.813	Simonin	0.959	0.849	5294.5
73	0.950	K-Epsilon	0.846	0.831	4064.1
74	0.950	K-Epsilon	0.880	0.982	4027.4
75	0.950	K-Epsilon	0.884	0.904	3940.0
76	0.950	K-Epsilon	0.906	0.829	3994.6
77	0.950	K-Epsilon	0.964	0.877	3955.9
78	0.950	K-Epsilon	0.979	0.975	3997.1
79	0.950	Laminar	0.800	0.979	4840.0
80	0.950	Laminar	0.882	0.951	4844.8
81	0.950	Laminar	0.911	0.895	4849.5
82	0.950	Laminar	0.946	0.928	4777.0
83	0.950	Laminar	0.966	0.800	4736.7

84	0.950	Laminar	0.990	0.948	4628.9
85	0.950	Simonin	0.820	0.882	Did Not Reach Steady State
86	0.950	Simonin	0.840	0.964	4849.7
87	0.950	Simonin	0.877	0.926	4834.5
88	0.950	Simonin	0.900	0.811	4758.1
89	0.950	Simonin	0.928	0.913	4847.1
90	0.950	Simonin	0.962	0.873	4693.3

Appendix 2

Variables

B	Bernoulli Polynomial
C_D	single particle drag function (-)
Cp	specific heat (J/kg·K)
D	rate of strain (1/s)
G	acceleration due to gravity (m/s^2)
G_n	number of categorical variables (-)
h	heat transfer coefficient (W/m^3K)
I	indicator function
$\bar{I}$	unit tensor (-)
k	thermal conductivity (W/m·K)
K	covariance terms
l	bed width (m)
L	characteristic filter size (-)
P	pressure (Pa)
Re	Reynolds Number (-)
T	temperature (K)
$\tilde{T}$	mass weighted temperature (K)
u	velocity (m/s)
q_Θ	diffusive flux of granular energy ($J/m^2 \cdot s$)
Q	heat flux ($W/m^3 \cdot K$)
x	model input
y	model output

Greek Letters

α_o	model intercept (-)
β	interphase momentum exchange coefficient (-)
γ_Θ	granular energy dissipation ($J/m^3 \cdot s$)
γ_{gs}	interphase heat transfer coefficient (W/m^3K)
δ	model discrepancy term
ε_n	observation error
η	emulator
θ	model parameter
Θ	granular temperature (m^2/s^2)
κ	bed fluidization pressure (Pa)
λ	variance due to categorical terms
μ	viscosity (kg/m·s)
υ	coefficient of restitution (-)
Π	interphase exchange of granular energy ($J/m^3 \cdot s$)
Π_s	heat generation (K/s)

ρ	density (g/cm^3)
ς	variance due to continuous terms
τ	stress (Pa)
Φ	phase fraction, volume (-)
ω	vector of model inputs

Subscripts

i,j,k	Rectangular Coordinate Axes
g	Gas Phase
s	Solid Phase

Bibliography

[1] Kapil Agrawal, William Holloway, Christian C. Milioli, Fernando E. Milioli, and Sankaran Sundaresan, "Filtered models for scalar transport in gas-particle flows," *Chemical Engineering Science*, no. 95, pp. 291–300, 2013.

[2] K. Agrawal, P. N. Loezos, M. Syamlal, and S. Sundaresan, "The role of meso-scale structures in rapid gas-solids flows," *Journal of Fluid Mechanics*, vol. 445, pp.151–185, 2001.

[3] Michael Allaby, *Oxford dictionary of earth sciences*. Oxford University Press, 2008.

[4] G. Balzer, O. Simonin, A. Boelle, and J. Lavieville, "Unifying modelling approach for the numerical prediction of dilute and dense gas-solid two phase flow," in *5th International Conference on Circulating Fluidized Beds*, Beijing, China, 1996.

[5] Sofiane Benyahia. (2009) MFIX Mailing Lists. [Online]. https://mfix.netl.doe.gov/sympa/arc/mfix-help/2009-03/msg00036.html

[6] S. Benyahia, M. Syamlal, and T.J. O'Brien. (2012, January) Summary of MFIX Equations 2012-1. [Online]. https://mfix.netl.doe.gov/download/mfix/mfix_current_documentation/MFIXEquations2012-1.pdf

[7] Sofiane Benyahia, Madhava Syamlal, and Thomas J. O'Brien, "The effect of model parameters on the predictions of core-annular flow behavior in a fast-fluidized gas/solids bed," Unpublished paper presented at the AIChE Annual Meeting, 2004, Austin, TX, paper 289d.

[8] J. Cao and G. Ahmadi, "Gas-particle two-phase turbulent flow in a vertical duct," *International Journal of Multiphase Flow*, vol. 21, no. 6, pp. 1203–1228, 1995.

[9] (2014) CHEMICAL REACTION ENGINEERING. [Online]. http://classes.engineering.wustl.edu/che471/Fluidized%20bed%20introduction.pdf

[10] (2013, June) DOE/NETL ADVANCED CO2 Capture R&D PROGRAM: TECH UPDATE. [Online]. http://www.netl.doe.gov/research/coal/carbon-capture/capture-handbook

[11] A. D. Ebner et al., "Suitability of a Solid Amine Sorbent for CO2 Capture by Pressure Swing Adsorption," *Industrial and Engineering Chemistry Research*, vol. 50, no. 9, pp. 5634–5641, 2011.

[12] Dimitri Gidaspow, *Multiphase Flow and Fluidization: Continuum and Kinetic Theory Descriptions*. Academic Press, 1994.

[13] C. M. Hrenya, R. Cocco, R. Fox, S. Subramaniam, and S. Sundaresan, "Final Technical Report on Development, Verification, and Validation of Multiphase Models for Polydisperse Flows," (NETL) National Energy Technology Laboratory, University of Colorado. 2011.

[14] Christine M. Hrenya and Jennifer L. Sinclair, "Effects of particle-phase turbulence in gas-solid flows," *AlChE Journal*, vol. 43, no. 4, pp. 853–869, 1997.

[15] D. E. Huntington and C. S. Lyrintzis, "Improvements to and limitations of Latin hypercube sambling," *Probabilistic Engineering Mechanics*, vol. 13, no. 4, pp. 245–253, 1998.

[16] Yesim Igci and Sankaran Sundaresan, "Constitutive Models for Filtered Two-Fluid Models of Fluidized Gas–Particle Flows," *Industrial & Engineering Chemistry Research*, vol. 50, no. 23, pp. 13190–13201, 2011.

[17] P. C. Johnson and R. Jackson, "Frictional–collisional constitutive relations for granular materials, with application to plane shearing," *Journal of Fluid Mechanics*, vol. 176, pp. 67–93, 1987.

[18] W. A. Lane, E. M. Ryan, A. Sarkar, and S. Sundaresan, "Sub-grid filtering of heat transfer in gas-solid flows with immersed heat transfer cylinders," in *ASME International Mechanical Engineering Congress & Exposition*, Montreal, Canada, 2014.

[19] William A. Lane, Curtis B. Storlie, Christopher J. Montgomery, and Emily M. Ryan, "Numerical modeling and uncertainty quantification of a bubbling fluidized bed with immersed horizontal tubes," *Powder Technology*, vol. 253, pp. 733–734, 2014.

[20] Claudio Maccone, *Deep Space Flight Comunications*. Springer Berlin Heidelberg, 2009.

[21] (2015, March) Multiphase Flow Science. [Online]. https://mfix.netl.doe.gov/

[22] Khalid Osman, Christophe Coquelet, and Deresh Ramjugernath, "Review of carbon dioxide capture and storage with relevance to the South African power sector," *South African Journal of Science*, vol. 110, no. 5–6, pp. 1–12, 2013.

[23] Brian J. Reich, Curtis B. Storlie, and Howard D. Bondell, "Variable selection in Bayesian smoothing spline ANOVA models: Application to deterministic computer codes," *Technometrics,* vol. 51, no. 2, pp. 110–120, 2009.

[24] Joseph V. Roshan and Hung Ying, "Orthogonal-Maximin Latin Hypercube Designs," *Statistica Sinica*, vol. 18, pp. 171–186, 2008. [Online]. http://www3.stat.sinica.edu.tw/statistica/oldpdf/A18n17.pdf

[25] A. Saltelli, K. Chan, and E. Scott, *Sensitivity Analysis*. New York, NY: Wiley, 2000.

[26] Avik Sarkar, Xin Sun, and Sankaran Sundaresan, "Sub-grid drag models for horizontal cylinder arrays immersed in gas-particle multiphase flows," *Chemical Engineering Science*, vol. 104, pp. 399–412, 2013.

[27] Abdelhamid Sayari and Youssef Belmabkhout, "Stabilization of Amine-Containing CO2 Adsorbents: Dramatic Effect of Water," *Journal of the American Chemistry Society*, vol. 132, no. 18, pp. 6312–6314, 2010.

[28] (2015, January) Significant speedup and enhanced modeling capabilities achieved in MFIX. [Online]. https://mfix.netl.doe.gov/?p=1747

[29] I. M. Sobol, "Global sensitivity indices for nonlinear mathematical models and their Monte Carlo estimates," *Mathematics and Computers in Simulation*, vol. 55, no. 1–3, pp. 271–280, 2001.

[30] C. Song, P. Wang, and H. A. Makse, "A phase diagram for jammed matter," *Nature*, vol. 453, pp. 629–632, 2008.

[31] Curtis Storlie, BSS-ANOVA-UQ: A Calibration/Validation UQ Tool for Expensive Computer Models, 2013, Los Alamos National Laboratory.

[32] Curtis B. Storlie, William A. Lane, Emily M. Ryan, James R. Gattiker, and David M. Higdon, "Calibration of Computational Models with Categorical Parameters and Correlated Outputs via Bayesian Smoothing Spline ANOVA," *Journal of the American Statistical Association* (in press) (2015).

[33] Curtis B. Storlie, Brian J. Reich, Jon C. Helton, Laura P. Swiler, and Cedric J. Sallaberry, "Analysis of computationally demanding models with continuous and categorical inputs," *Reliability Engineering and System Safety*, vol. 113, pp. 30–41, 2013.

[34] S. Subramaniam, "Lagrangian–Eulerian methods for multiphase flows," *Progress in Energy and Combustion Science*, vol. 39, pp. 215–245, 2013.

[35] M. Syamlal, "A Review of Granular Stress Constituitive Relations," Springfield, VA, 1987.

[36] Madhava Syamlal, William Rogers, and Thomas J. O'Brien, "MFIX Documentation Theory Guide," Department of Energy, Morgantown, WV, Technical Note DE94000087, 1993.

[37] (2015) The R Project for Statistical Computing. [Online]. http://www.r-project.org/

[38] Li Tingwen, Jean-François Dietiker, Yongmin Zhang, and Mehrdad Shahnam, "Cartesian grid simulations of bubbling fluidized beds with a horizontal tube bundle," *Chemical Engineering Science*, vol. 66, no. 23, pp. 6220–6231, 2011.

[39] S. Ulam, "The Monte Carlo Method," *Journal of the American Statistical Association*, vol. 44, no. 247, pp. 335–341, 1949.

[40] R. Veneman, Z. S. Li, J. A. Hogendoorn, S. R. A. Kersten, and D. W. F. Brilman, "Continuous CO2 capture in a circulating fluidized bed using supported amine sorbents," *Chemical Engineering Journal*, vol. 207–208, pp. 18–26, 2012.

[41] Annemarie Wagner et al., "Carbon Dioxide Capture from Ambient Air Using Amine-Grafted Mesoporous Adsorbents," *International Journal of Spectroscopy*, 2013. http://dx.doi.org/10.1155/2013/690186

[42] Ying Xu and Shankar Subramaniam, "A multiscale model for dilute turbulent gas-particle flows based on the equilibration of energy concept," *Physics of Fluids*, vol. 18, no. 3, p. 033301, 2006.

Curriculum Vitae

Christopher J. Moulder
7 Unity Street #2 • Boston, MA 02113
952-200-0040 • CMoulder@alum.rpi.edu

EDUCATION

Boston University (BU), Boston, MA — Expected: May 2015
M.S. Mechanical Engineering

Rensselaer Polytechnic Institute (RPI), Troy, NY — Graduated: May 2010
B.S. Aeronautical and Mechanical Engineering, Magna Cum Laude

EXPERIENCE

GE Aviation, Lynn, MA — Aug 2011 - Present
Edison Engineering Development Program

- Construct analytical risk models and fleet monitoring plans to guarantee aircraft engine safety and reliability to government regulators
- Evaluate manufacturing quality escapes with statistical analysis to avert fleet groundings
- Created statistical model and optimized process parameters to improve yield from 7% to 28% for key next generation airfoil technology
- Generated a new engine performance model to match field test data within 3% and to provide 3-sigma production margins while meeting contract requirements

Air Force Flight Test Center, Edwards AFB, CA — June 2010 - July 2011
Propulsion Flight Test Engineer

- Analyzed flight test data and provided documentation for Air Force certification of biofuels on the C-17 Aircraft
- Developed case studies detailing statistically sound analysis methods congruent with Air Force Design of Experiment initiatives
- Wrote engine performance module for the Society of Flight Test Engineers Handbook

LEADERSHIP

River Works Credit Union, Lynn, MA — Nov 2013 - Present
Director

- Administer governance of a growing credit union with $100 million in assets
- Provide oversight related to regulatory compliance and contribute to the development of a strategic plan in conjunction with other board members

Toastmasters International, Lynn, MA — 2013
Treasurer

- Managed memberships, tracked club finances, and acquired funding for 40 members
- Organized agenda and conducted designated club meetings

GE Aviation Product Engineering Center, Lynn, MA 2013
Edison Council Member
- Selected to lead Edison community engagement events by program leadership
- Led five events including Speed Networking to introduce Edisons to hiring managers

GE Aviation Product Engineering Center, Lynn, MA 2012 - 2013
Productivity and Simplification Champion
- Coordinated brainstorming sessions and managed process improvement ideas for onsite design teams
- Presented top improvement ideas to the senior leadership team

DISTINCTIONS

GE Advanced Courses in Engineering 2011 - 2013
- Completed A & B Course

Department of Defense SMART Scholarship Award Recipient 2009 - 2010
- A highly competitive scholarship established by the DOD for students in STEM fields

Boy Scouts of America: Eagle Scout 2003